mathematics

MDPI

Article

A Fractal Analysis of the Size Effect in Quasi-Brittle Materials: Experimental Tests and Peridynamic Simulations

Leandro Ferreira Friedrich [1,*], Luis Eduardo Kosteski [1], Édiblu Silva Cezar [2], Angélica Bordin Colpo [1], Caroline Bremm [1], Giuseppe Lacidogna [2] and Ignacio Iturrioz [3]

[1] MAEC Group, Post-Graduation Program of Federal University of Pampa, Av. Tiaraju 810, Alegrete 97546-550, CEP, Brazil; luiskosteski@unipampa.edu.br (L.E.K.); angelicacolpo@unipampa.edu.br (A.B.C.); carolinebremm.aluno@unipampa.edu.br (C.B.)
[2] Department of Structural, Geotechnical and Building Engineering, Politecnico di Torino, 24, Corso Duca degli Abruzzi, 10129 Torino, Italy; ediblu.silvacezar@polito.it (É.S.C.); giuseppe.lacidogna@polito.it (G.L.)
[3] Mechanical Post-Graduate Program, Federal University of Rio Grande do Sul, Sarmento Leite 425, Porto Alegre 90050-170, CEP, Brazil; ignacio.iturrioz@ufrgs.br
* Correspondence: leandrofriedrich@unipampa.edu.br

Abstract: In the design of structures involving quasi-brittle materials such as concrete, it is essential to consider the scale dependence of the mechanical properties of the material. Among the theories used to describe the phenomenon of size effect, the fractal theory proposed by Carpinteri and colleagues has attracted attention for its results in the last three decades of research. The present study employs the fractal perspective to examine the scale effect in three-point bending tests conducted on expanded polyethylene (EPS) beam specimens. The influence of size on flexural strength, fracture energy, and critical angle of rotation is investigated. Additionally, numerical simulations based on peridynamic (PD) theory are performed based on the experimental tests. The global behavior, brittleness, failure configuration, and fractal scale effect obtained numerically are evaluated. The numerical results show a good correlation with the experimental ones and, moreover, both the experimental and numerical results are in agreement with the fractal theory of scale effect. More precisely, the error of the sum of the fractal exponents, computed with respect to the theoretical one, is equal to −1.20% and −2.10% for the experimental and numerical results, respectively. Moreover, the classical dimensional analysis has been employed to demonstrate that the scale effect can be naturally described by the PD model parameters, allowing to extend the results for scales beyond those analyzed experimentally.

Keywords: size effect; fractal approach; peridynamic; dimensional analysis

MSC: 74A70; 74A40; 74A45

check for updates

Academic Editors: Miguel Ángel Sánchez-Granero and Theodore E. Simos

Received: 28 September 2024
Revised: 9 December 2024
Accepted: 27 December 2024
Published: 29 December 2024

Citation: Friedrich, L.F.; Kosteski, L.E.; Cezar, É.S.; Colpo, A.B.; Bremm, C.; Lacidogna, G.; Iturrioz, I. A Fractal Analysis of the Size Effect in Quasi-Brittle Materials: Experimental Tests and Peridynamic Simulations. *Mathematics* **2025**, *13*, 94. https://doi.org/10.3390/math13010094

Copyright: © 2024 by the authors. Licensee MDPI, Basel, Switzerland. This article is an open access article distributed under the terms and conditions of the Creative Commons Attribution (CC BY) license (https://creativecommons.org/licenses/by/4.0/).

1. Introduction

The damage process in quasi-brittle materials, including rocks, concrete, ceramics, and some polymers reinforced by fibers, is a complex phenomenon involving a wide range of scale and assuming lengths. The nucleation, growth, and coalescence of internal defects of varying kinds, shapes, and sizes can lead the material to the final collapse catastrophically. Furthermore, a significant challenge arises from the sample-size dependence, that is, the size effect of certain material properties (such as nominal strength, fracture energy, and deformation at failure [1]), which makes it difficult to accurately predict the behavior of large structures based on laboratory tests on similarly shaped samples [2,3].

Different approaches have been proposed to solve the size effect problem over the past 40 years. Some examples of these approaches are the size effect law (SEL) proposed by Bazant and colleagues [4–6], the fractal scale approach proposed by Carpinteri and colleagues [7–10], and the Krajcinovic approach proposed by Rinaldi and Mastilovic [11].

Regarding the fractal approach employed in this work, Carpinteri and coworkers have shown that fracture in quasi-brittle materials, and more precisely the variation of their properties with their size, is better described by considering fractal dimensions rather than the traditional Euclidean dimensions, which are integers [12]. In fractal geometry, the dimensions are not integers but fractional, which reflects the complexity and self-similarity of fracture surfaces at different scales [13]. In fact, experimental evidences confirm that on the fracture surface of many materials, fractal shapes can be observed, such as in metals, ceramics, concrete, and rocks, among others [13,14]. According to the fractal size effect, the measurement of the variation of a mechanical property (Q) is carried out through the so-called fractal exponents, dQ, described by a power law in general terms as:

$$Q = Q^* b^{dQ} \tag{1}$$

where Q^* is the scale invariant material property and b is a characteristic dimension of the structure. The range of variations observed in fractal exponents is dependent upon a number of factors, including the geometrical shape of the specimens, the boundary conditions, the characteristics of the material (in particular, the maximum aggregate size and quantities in the concrete, for example), and other variables [15]. In Refs. [7,8,10,13,16–19], it was demonstrated that the fractal exponent of tensile stress varies between 0.091 and 0.41, the fractal exponent of fracture energy varies between 0.085 and 0.48, and the fractal exponent of critical strains varies between 0.48 and 0.73. In the context of three-point bending tests, the exponent values, according to the studies conducted by Carpinteri and Accornero [20] and Lacidogna et al. [21], are in the range of 0.1 to 0.3 for flexural strength, 0.1 to 0.3 for fracture energy, and 0.2 to 0.5 for the critical rotation angle (which has the same meaning as the critical strain for the tensile test).

The size scale effects on the mechanical properties in quasi-brittle materials has been investigated in numerous experimental studies over decades under different kinds of loading such as compression [22,23], tension [15,24,25], flexure [20,21,26], shear [27], and torsion [28]. In order to help and complement the understanding of this phenomenon, a number of numerical models have been proposed over the years. Such models can be divided, in general terms, into two broad categories according to their approach. The first category comprises models based on continuum mechanics, which can be considered a classical approach, including those based on the Finite Element Method (FEM), such as the Cohesive Zone Model [29], X-FEM [30] and Phase-Field [31]. The second category includes statistically based models that assume a random nature for the microstructure of the material, such as, for example, the Discrete Element Method (DEM) [32–34]. Continuum mechanics-based models incorporate damage variables or damage evolution laws into the equations describing mechanical fields [35]. On the other hand, the DEM has been applied with the same role, but allowing more shapes, sizes, materials, and other parameters to be studied, as can be seen in Refs. [36,37].

An alternative to the above approaches is a model based on the peridynamic (PD) theory, which is an integral-type non-local theory initially proposed by Silling [38]. The efficacy of PD as a modelling tool for cracking and failure processes in solid bodies has been increasingly acknowledged in recent years [39,40]. The governing equation of PD can keep valid even when discontinuities or cracks occur. Another advantage of PD is that the damage process and crack propagation can be spontaneously predicted without other extra crack propagation criteria as the re-meshing approach [41], for example.

In the context of simulation of quasi-brittle materials, some applications of PD are present in the recent literature, such as in Refs. [42–47]. In particular, in the case of the size effect, few works are found. In Hobbs et al. [48], the size effect in quasi-brittle materials using a three-dimensional peridynamic model was examined. Geometrically similar beams of different sizes were modeled to examine the size effect on structural strength based on the SEL approach. Notched and unnotched beams were modeled to examine the effect of boundary types on the predictive accuracy of the peridynamic model, and mode I and mixed-mode problems were considered. In Bazant et al. [49], the performance of PD theory in studying the scale effect of concrete beams was criticized by the authors, claiming that PD cannot reproduce the transitional size effect, which is an essential characteristic of quasi-brittle materials.

In this context, the present work focuses on analyzing the scale effect of quasi-brittle materials based on the fractal approach through experimental tests and numerical simulations using peridynamics. To the best of the authors' knowledge, this is the first time that PD models have been applied to investigate the fractal scale effect. The experimental tests were carried out on scaled expanded polystyrene (EPS) beam specimens subjected to three-point bending tests. By employing a PD approach for quasi-brittle materials, based on the first version of the PD theory, named the bond-based peridynamic theory, tridimensional PD models were used to simulate the experimental tests. Both experimental and numerical results were compared in terms of global behavior, brittleness, failure configuration, and the fractal scale effect on the flexural strength, fracture energy, and critical rotation angle. Moreover, the classical dimensional analysis is employed to demonstrate that the scale effect can be described by the PD model parameters, allowing the results to extend to extreme cases for large and small samples.

2. A Bilinear PD Model for Quasi-Brittle Materials

In this section, firstly, a concise overview of the bond-based PD theory is presented. Then, the bilinear PD model (named BPD model in the following) recently proposed in Friedrich et al. [46] for failure analysis of quasi-brittle material is presented. The main features of this model are the implementation of: (i) a bilinear bond force–stretch relationship, and (ii) the random field for the fracture energy.

2.1. Basic Concepts of the Bond-Based Peridynamic Theory

The PD theory discretizes a solid body subjected to external loads into material particles, each of them surrounded by a neighborhood known as the peridynamic horizon, δ_0. Figure 1a illustrates the kinematics of a typical PD body.

The force of interaction between material particle $\boldsymbol{x}$ and any neighboring particle $\boldsymbol{x}'$ in the horizon (i.e., $\boldsymbol{x}' \in H_x$, as illustrated in Figure 1a) is defined by the pairwise force density function $\boldsymbol{f}$. This function is measured as a force per unit volume and represents the force vector exerted by particle $\boldsymbol{x}'$ on particle $\boldsymbol{x}$.

The governing PD equation of motion at time step t can be described as follows [50]:

$$\rho(\boldsymbol{x})\ddot{\boldsymbol{u}}(\boldsymbol{x},t) = \int_{H_x} \boldsymbol{f}(\boldsymbol{x}' - \boldsymbol{x}, \boldsymbol{u}(\boldsymbol{x}',t) - \boldsymbol{u}(\boldsymbol{x},t))dV_{\boldsymbol{x}'} + \boldsymbol{b}(\boldsymbol{x},t) \tag{2}$$

where ρ is the material mass density, $\boldsymbol{x}$ and $\boldsymbol{x}'$ are the position vectors, $\boldsymbol{u}$ and $\ddot{\boldsymbol{u}}$ are the displacement vector and the acceleration vector, $dV_{\boldsymbol{x}'}$ denotes an infinitesimal volume around the $\boldsymbol{x}'$ particle, and $\boldsymbol{b}$ is the body force density.

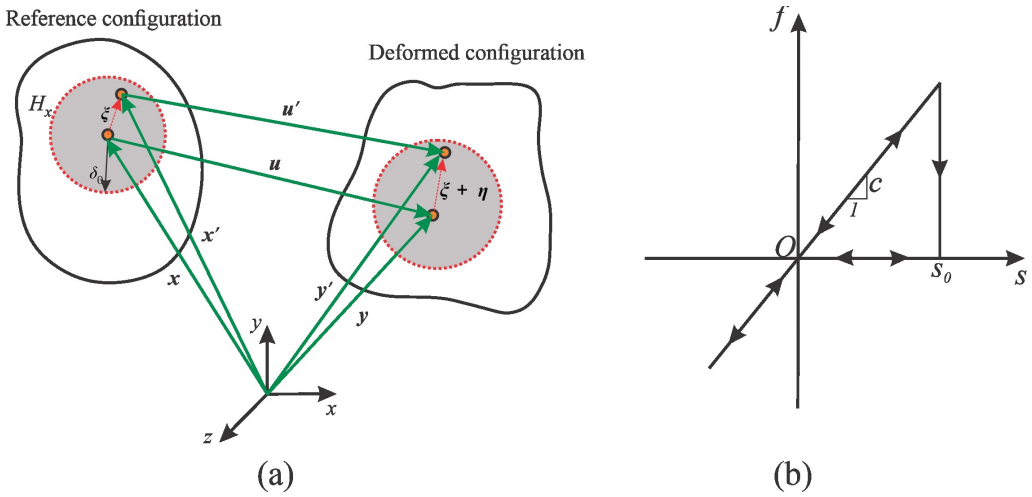


Figure 1. (**a**) Reference configuration and deformed configuration according to PD theory, (**b**) Prototype Microelastic Brittle (PMB) model.

The pairwise force density function, $\boldsymbol{f}$, for linear elastic materials, is given by [51]:

$$\boldsymbol{f} = f\frac{\boldsymbol{\xi}+\boldsymbol{\eta}}{|\boldsymbol{\xi}+\boldsymbol{\eta}|} \tag{3}$$

where $\boldsymbol{\xi}$ and $\boldsymbol{\eta}$ are the relative position vector and the relative displacement vector, respectively, defined as $\boldsymbol{\xi} = \boldsymbol{x}' - \boldsymbol{x}$ and $\boldsymbol{\eta} = \boldsymbol{u}' - \boldsymbol{u}$, and $f = cs$ is the scalar bond force density function, with c being the PD bond constant and s the scalar bond stretch.

The value of parameter c is determined by the Poisson ratio, which varies depending on whether the analysis is performed (fixed as $\nu = 0.25$ for three dimensional analysis and for two dimensional analysis under plane strain conditions, whereas it is fixed as $\nu = 1/3$ for two dimensional analysis under plane stress conditions) [50,51]:

$$c = \begin{cases} \frac{6E}{\pi\delta_0^4(1-2\nu)} & \text{3D analysis} \\ \frac{6E}{\pi h\delta_0^3(1-\nu)} & \text{2D analysis—plane stress} \\ \frac{6E}{\pi h\delta_0^3(1-2\nu)(1+\nu)} & \text{2D analysis—plane strain} \end{cases} \tag{4}$$

where E is the elastic modulus, h is the thickness, and δ_0 represents the horizon size. In the PD model implementation, generally δ_0 is defined as the radius of a circle for 2D problems or the radius of a sphere for 3D problems.

The bond stretch, s, is given by:

$$s = \frac{|\boldsymbol{\xi}+\boldsymbol{\eta}| - |\boldsymbol{\xi}|}{|\boldsymbol{\xi}|} \tag{5}$$

To describe brittle fracture, the Prototype Microelastic Brittle (PMB) model is widely adopted, as shown in Figure 1b [51]. According to this model, the function f is described as:

$$f = \varphi cs \tag{6}$$

where φ is given by:

$$\varphi = \begin{cases} 1 \text{ if } s < s_0 \\ 0 \text{ if } s \geq s_0 \end{cases} \tag{7}$$

with s_0 being the critical bond stretch (see Figure 1b), which can be computed as [46,51]:

$$s_0 = \sqrt{\frac{RG_f}{E\delta_0}} \tag{8}$$

where G_f is the material fracture energy, R is equal to $5/6$ for 3D analysis, and $4\pi/9$ and $5\pi/12$ for 2D plane stress and plain strain analysis, respectively [46].

Based on Equation (7), a local damage index ϑ, which can be used to observe the crack path, can be defined as,

$$\vartheta(\boldsymbol{x}, t) = 1 - \frac{\int_{H_x} \varphi dV_\xi}{\int_{H_x} dV_\xi} \tag{9}$$

2.2. A PD Approach for Quasi-Brittle Materials

According to recommendations [51,52], a minimum of three material particles must exist within the horizon (δ_0) in order to guarantee good precision in the results. Therefore, a minimum particle spacing is necessary, Δ (assumed to be equal in the three coordinate directions x, y, and z), equal to $\delta_0/3.015$. If a smaller discretization needs to be applied while maintaining the previous δ_0 value, then the number of particles within the horizon will increase, which would lead to simulations with higher computational cost. The BPD model, initially introduced by Cabral et al. [43] and further improved by Friedrich et al. [46], was developed in response to this issue. More specifically, two horizons are defined in the BPD formulation: δ', which is independent of the chosen Δ and that assumes the concept of material property (which will be defined in the following), and δ_0, which is a parameter that depends only on the model discretization and has a fixed relation with the discretization level, $\delta_0 = 3.015\Delta$. The key aspect of the BPD model is the correlation between δ' and δ_0, as it allows simulating the same material behavior with different levels of discretization; i.e., it is possible to use different δ_0 while maintaining the same δ'.

Contrasting with the classic PMB model presented in the previous section, the BPD model presents a linear softening branch, allowing to capture the post-peak softening behavior inherent to quasi-brittle materials. In Cabral et al. [43] and Friedrich et al. [46], several numerical results were compared with experimental ones showing the capabilities of such model. Furthermore, the equivalence between the PMB model utilizing $\delta_0 = \delta'$ and the BPD model has been verified in Cabral et al. [43].

The bilinear bond force–stretch relationship is shown in Figure 2, where the parameters characterizing such a relationship are:

- the loading branch slope, c (see Equation (4));
- the maximum elastic stretch, s_p, being the strain at the material elastic limit (see Friedrich et al. [46,47] for details);
- the rupture stretch, s_r, defined as:

$$s_r = K_r s_p \tag{10}$$

where K_r governs the shape of the softening branch (red line in Figure 2).

In the BPD model, it is proposed that parameter K_r should be calculated by equating the area underlying both the PMB model (Figure 1b) and the bilinear one (Figure 2), that is:

$$s_0{}^2 = s_p s_r = K_r s_p{}^2 \tag{11}$$

By computing the critical stretch corresponding to the PMB model when δ' is employed (replacing δ_0 by δ' in Equation (8)), the following relation is obtained:

$$s' = \sqrt{\frac{RG_f}{E\delta'}} \tag{12}$$

and by replacing Equation (11) into Equation (8) and exploiting Equation (12), the following relation is obtained:

$$K_r \, s_p^2 \, \delta_0 = s'^2 \, \delta' \tag{13}$$

The K_r parameter, as computed using Equation (13), establishes a connection between the numerical horizon (δ_0) and the material horizon (δ'). It is worth noting that ensuring stability in the formulation requires K_r to be greater than 1.0.

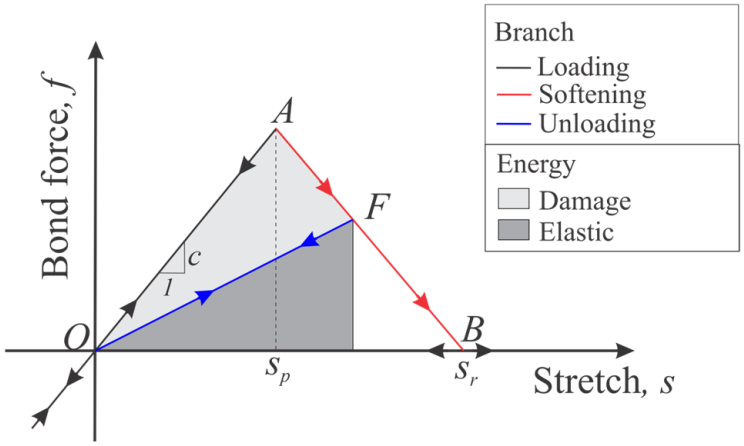


Figure 2. Bilinear bond force–stretch relationship used to model the quasi-brittle material behavior.

The horizon material property, δ', is calculated by exploiting concepts of the Linear Elastic Fracture Mechanics (LEFM). Let us consider Equation (12) and the relation between the critical stress intensity factor under mode I, K_{Ic}, and the fracture energy, G_f (that is, $K_{Ic} = \sqrt{G_f E}$). Such an equation can be rewritten as:

$$\delta' = \frac{R}{s'^2}\left(\frac{K_{Ic}}{E}\right)^2 \tag{14}$$

By considering a crack problem under pure opening Mode I loading, that is, $K_{Ic} = \sigma_0 Y\sqrt{\pi a_c}$ and assuming the failure stress $\sigma_0 = Es'$, δ' can be computed from Equation (14) as:

$$\delta' = RY^2\pi a_c \tag{15}$$

where Y is the geometric shape function, depending on the geometry of the cracked body, and a_c is the crack length at failure (critical crack size). If for simplicity, we assume that $RY^2\pi \approx 1$, then the horizon can be understood as a critical crack size, $\delta' \approx a_c$.

Based on the above concept, Figure 3 shows the behavior of a structure considering the presence of a given crack of size d. If d is smaller than the horizon, δ', case (i), then it is possible for the crack propagates unstable, and brittle behavior is expected. On the other hand, if the crack d is larger than the horizon, case (ii), then this crack does not enter inside the horizon and ductile failure occurs.

To compute δ' a procedure exploiting the concept of the so-called Theory of Critical Distance (TCD), introduced by Taylor [53], is here employed. More precisely, according to the TCD, the failure of a body containing a stress concentration (as for example, a crack or

a notch) can be predicted by using elastic stress information in a critical region close to the crack tip or the notch root. More precisely, such a critical region is here defined in terms of the characteristic material length by Taylor, named L_E, and given by:

$$L_E = \frac{1}{\pi}\left(\frac{K_{Ic}}{\sigma_0}\right)^2 \tag{16}$$

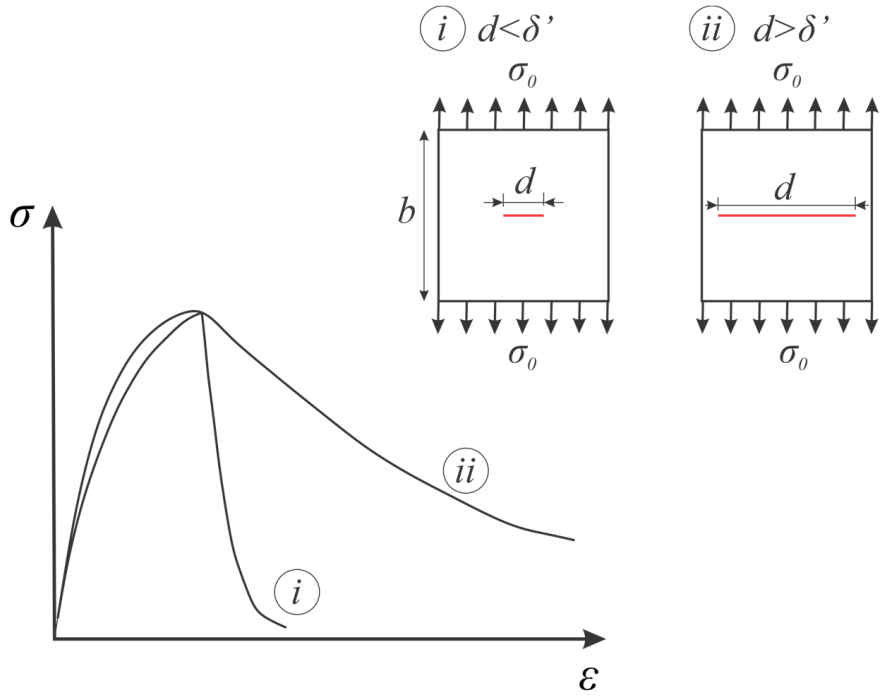


Figure 3. Schematic representation of the physical meaning of the horizon (δ') in the PD approach for quasi-brittle materials.

By combining Equation (14) with Equation (16) and assuming again, $\sigma_0 = Es'$, then δ' is given by:

$$\delta' = RL_E\pi \tag{17}$$

where the value of L_E is available in the literature for many materials [53]. Moreover, when the value of L_E is not available, it can be defined by exploiting the microstructural characteristics of the material such as the grain size in metals and ceramics and the aggregate size, for example, in concrete [54].

On the BPD model the unloading branch is characterized by the absence of residual strain (see the solid blue line in Figure 2) and under compression, the f–s relationship is linear elastic.

In the BPD model, the scalar bond function (Equation (7)), φ, is given by:

$$\varphi = \begin{cases} 1 & s < s_p \\ \frac{area\ OFB}{area\ OAB} & s_p \le s \le s_r \\ 0 & s < s_r \end{cases} \tag{18}$$

where the above areas are graphically defined in Figure 2 in order to compute the elastic and damage energy.

It is worth noticing that the bilinear bond force–stretch relationship presented in Figure 2 is also implemented in other PD models available in the literature. For example, it can be seen in the Micropolar Peridynamic Model proposed by Gerstle et al. [55] and in the

fully homogenized peridynamic model by Niazi et al. [56], and the PD framework based on the global arc-length method proposed by Sheikhbahaei et al. in Ref. [57] also employs this relationship.

To consider heterogeneous materials, different approaches have been employed in the context of peridynamic theory; see for example, the Intermediately Homogenized PeriDynamic (IH-PD) model [58–60] and random fields [46,47], with the latter being employed in this work. Specifically, a three-dimensional random field for the fracture energy has been implemented. More precisely, the linear spatial correlation of G_f is performed by dividing the domain into prismatic regions, each of them characterized by eight vertices and whose sizes are given by the correlation lengths, l_{cx}, l_{cy}, and l_{cz} along the three directions of a fixed reference frame x, y, and z, with a Weibull probability distribution being assumed along each of the above directions. The scaling and shape parameters of the Weibull distribution can be computed by means of a coefficient of variation, CV_{Gf}. The energy release rate for a generic bond i, $G_{f,i}$, identified by the coordinates of its barycenter (that is x_i, y_i and z_i), is calculated by using a 3D interpolation, performed on the G_f values related to the eight vertices of the prismatic region containing the generic bond, i. Consequently, as the parameters s_p and s_r are functions of G_f, the f–s relationship is different for each bond. More information regarding the 3D G_f random field can be found in Friedrich et al. [46].

Therefore, the input data, in addition to the geometrical sizes and boundary conditions characterizing the BPD model, are: Δ, E, ρ, s_p, G_f, and L_E. As far as the random field for G_f is concerned, l_{cx}, l_{cy}, l_{cz}, and CV_{Gf} have to be defined.

3. Materials and Methods

3.1. Description of the Experimental Tests

In order to analyze the size effect, unnotched beams with rectangular cross-sections are considered. The specimens were submitted to three-point bending testing, Figure 4a. Table 1 and Figure 4b show the average dimensions of the three sizes considered (with the depth of the beam, b, being the characteristic structural size), named in the following as Large (L), Medium (M), and Small (S). Tests were conducted under displacement-controlled mode up to final collapse, with the same strain rate maintained for all the sample sizes. The displacement rate is presented in Table 1 as well.

The mechanical and physical properties of the EPS constituting the beams are the following: mass density ρ = 11.9 kg/m^3 [46], elastic modulus E = 3.12 MPa [46], fracture energy G_f = 233.96 N/m [61], and flexural strength σ = 0.1 MPa. In order to characterize the material at the microstructural scale, a statistical analysis was performed in [61] to compute the average grain size of the EPS, obtaining its value equal to 5.02 mm.

Table 1. Average dimensions of specimens and displacement rate.

Dimensions and Test Speed	S	M	L
Span length, l [mm]	160	320	640
Depth, b [mm]	24	48	96
Width, e [mm]	16	32	64
Displ. rate [mm/min]	3.5	7.0	14

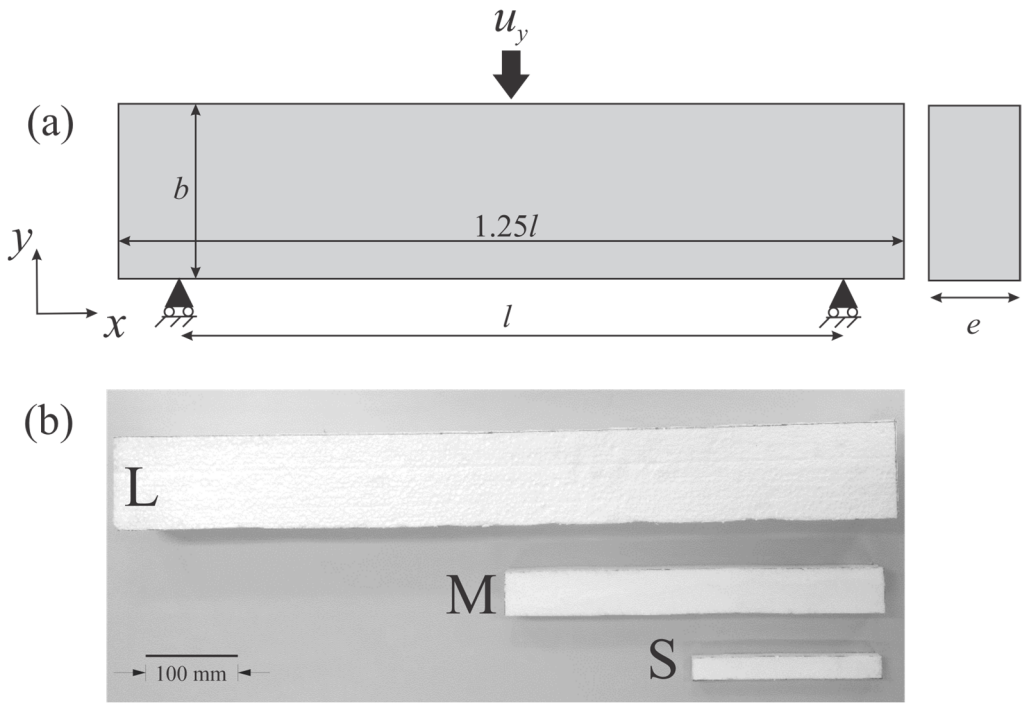


Figure 4. (**a**) Test setup and beams dimensions, (**b**) relative size of EPS specimens.

3.2. Numerical Models

The beams described above were numerically simulated by employing 3D PD models. The models consist of a number of particles along the x, y, and z direction, respectively, equal to 40 × 5 × 3 for the S size, 80 × 10 × 6 for the M size, and 160 × 19 × 13 for the L size. For all the specimen sizes, Δ is equal to 5 mm. Regarding the boundary conditions, see the example of the *L* size in Figure 5; the particles highlighted in blue on the left-hand side are constrained along the y direction, while those on the right-hand side are constrained along the x and y directions. On the particles located at the center of the beam, highlighted red in Figure 5, a uniform vertical displacement was applied in the y direction.

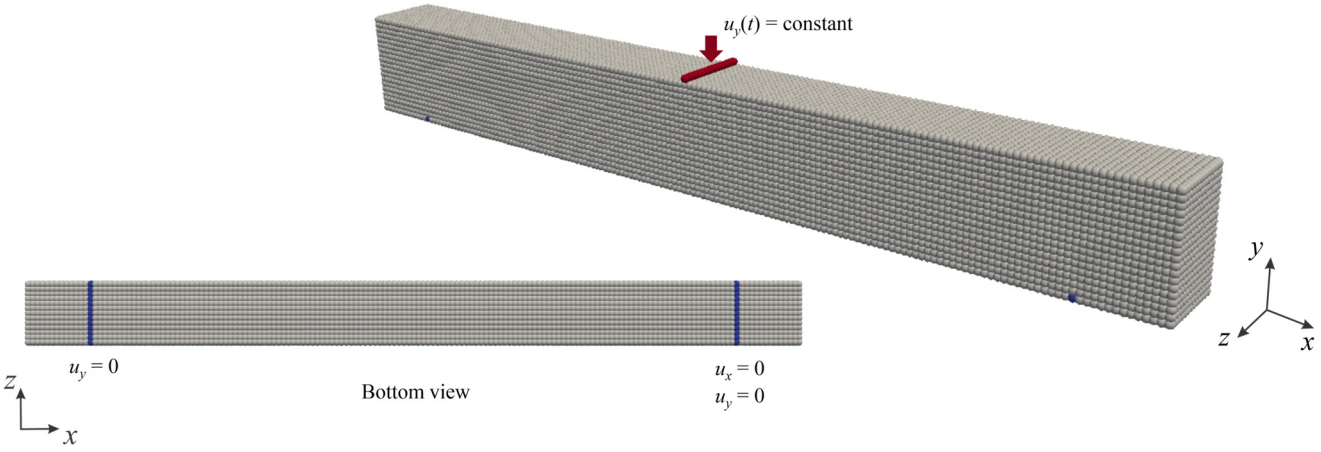


Figure 5. 3D PD model discretization and boundary conditions for the *L* size.

In Table 2 are summarized the parameters defining the bilinear PD model. By assuming Δ = 5.0 mm, δ_0 becomes equal to 15.075 mm. c is computed according to Equation (4) and resulting equal to 2.30 $(10)^{14}$ N/m^6. The parameter s_p is computed according to Section 2.1, that is, the strain in correspondence of the elastic limit (see details in Friedrich et al. [46]). δ' is computed according to Equation (17), where L_E, according to [46], is assumed to be

equal to three times the average grain size of the EPS and resulting equal to 40 mm. s', computed according to Equation (12), is equal to 0.0395. Therefore, K_r computed according to Equation (13), is equal to 71.76.

Table 2. Parameters defining proposed bilinear law.

Δ [mm]	δ_0 [mm]	c [N/m^6]	s_p [-]	δ' [mm]	s' [-]	K_r [-]
		Equation (3)	[48]	Equation (17)	Equation (12)	Equation (13)
5.0	15.075	2.3 (10)^{14}	0.0076	40.0	0.0395	71.76

Relatively to the 3D random field of the fracture energy, $l_{cx} = l_{cy} = l_{cz} = \Delta/2$. The coefficient of variation, CV_{Gf}, is taken to be equal to 30%. The above field was randomly generated four times for each beam size.

4. Results and Discussion

4.1. Global Behavior

The comparison between the experimental and numerical results is shown in Figure 6 in terms of flexural stress (σ) against flexural strain (ε) computed as:

$$\sigma = 6FS/tb^2 \tag{19}$$

$$\varepsilon = 6\mathrm{v}b/S^2 \tag{20}$$

where F is the load and v is the deflection measured by the displacement applied by the test machine. The curves No. refers to the different G_f random field generated.

In Table 3, the average flexural strength (σ) and the strain in correspondence to the above strength (ε) for the experimental tests and numerical simulations, together with their standard deviations, are reported. The error of the numerical results computed with respect to the average experimental ones (that is, error = (Exp − Num)/Exp) are presented as well. It can be observed that the numerical results are in good agreement with the experimental data in terms of both flexural strength and flexural strain. More precisely, the maximum errors for flexural strength and flexural strain, in absolute values, were achieved by the M beam size and are equal to 3.57% and 7.22%, respectively.

Moreover, a comparison of the experimental and numerical results reveals that the numerical results are valid up to the maximum flexural load, as evidenced by the greater softening observed in the experimental results, which is not reflected in the numerical data. This suggests that additional damage mechanisms may be at play, which the PD model is unable to fully capture.

Table 3. Experimental and numerical results in terms of flexural strength, σ, and flexural strain, ε, together with error of numerical values computed with respect to experimental ones.

		S	M	L
σ [MPa]	Exp.	0.0978 ± 0.0041	0.0931 ± 0.0025	0.0853 ± 0.0011
	Num.	0.1000 ± 0.0018	0.0898 ± 0.0008	0.0846 ± 0.0003
	Error	−2.24%	3.54%	0.82%
ε [-]	Exp.	0.103 ± 0.0059	0.084 ± 0.0045	0.057 ± 0.0037
	Num.	0.097 ± 0.0062	0.078 ± 0.0004	0.056 ± 0.0014
	Error	5.82%	7.14%	1.75%

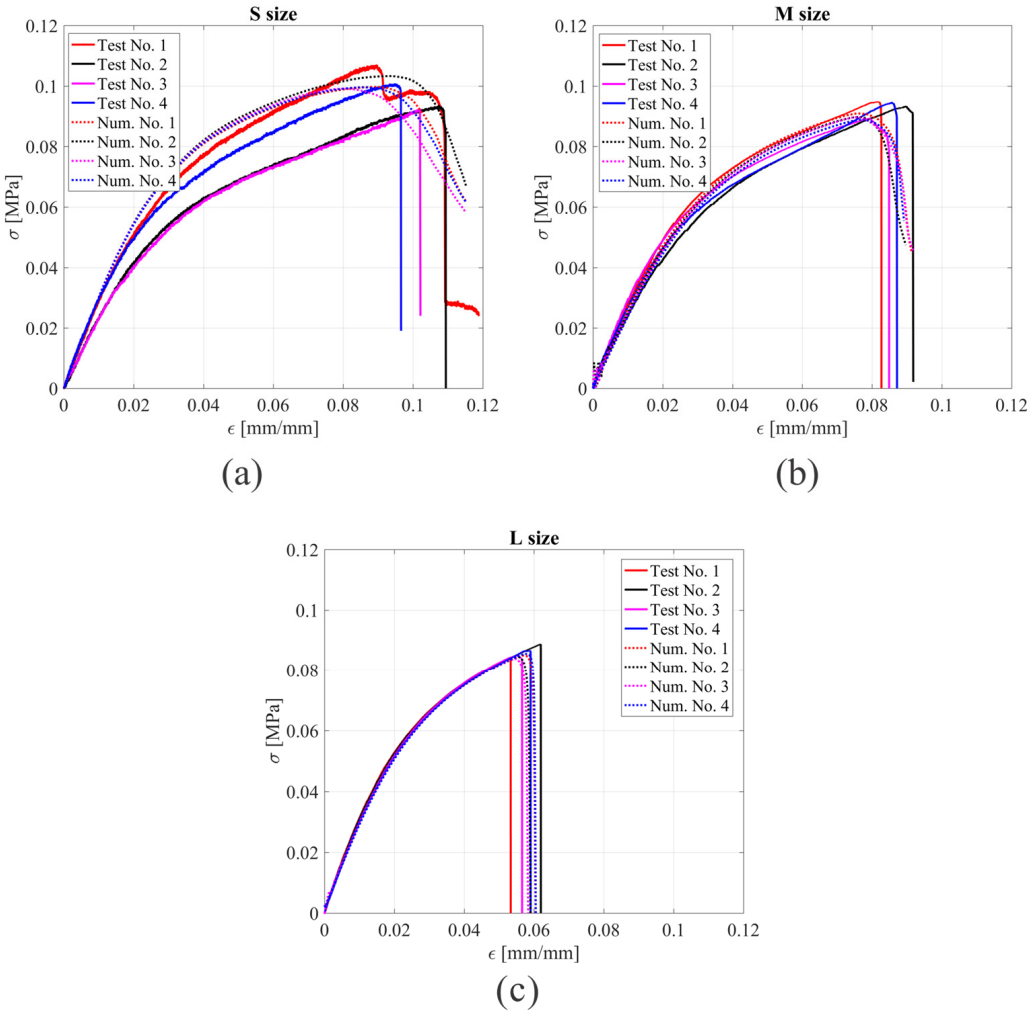


Figure 6. Experimental (solid lines) and numerical results (dotted lines) in terms of flexural stress-strain curves for: (**a**) small, (**b**) medium, and (**c**) large specimens.

In Figure 7, the ductile-to-brittle transition behavior is presented by exploiting a representative numerical force–deflection curve of each beam size. In order to measure the brittleness of the structure, a dimensionless parameter named stress brittleness number, n_f, proposed by Carpinteri [62], is here employed. Such a parameter is computed, in terms of the fracture energy, as:

$$n_f = \frac{\left(G_f E\right)^{0.5}}{\sigma_0 \sqrt{b}} \tag{21}$$

Based on experimental data and numerical simulations [63–67], the stress brittleness number values indicating brittle and ductile fracture behavior are $n_f < 1.0$ and $n_f > 1.5$, respectively.

By assuming b equal to the depth of the beam (see Table 1) and σ_0 equal to the average numerical flexural strength (see Table 3), the stress brittleness number, computed according to Equation (21), is equal to 1.68, 1.33, and 1.02 for S, M, and L size, respectively. Therefore, the behavior presented in Figure 6 and also that presented in Figure 5 for both experimental and numerical results are in agreement with respected to the predicted brittleness observed.

In Friedrich et al. [46], the previous Equation (21) was written in terms of the BPD model parameters as:

$$n_f^{PD} = \sqrt{\frac{\delta'}{Rb}} \tag{22}$$

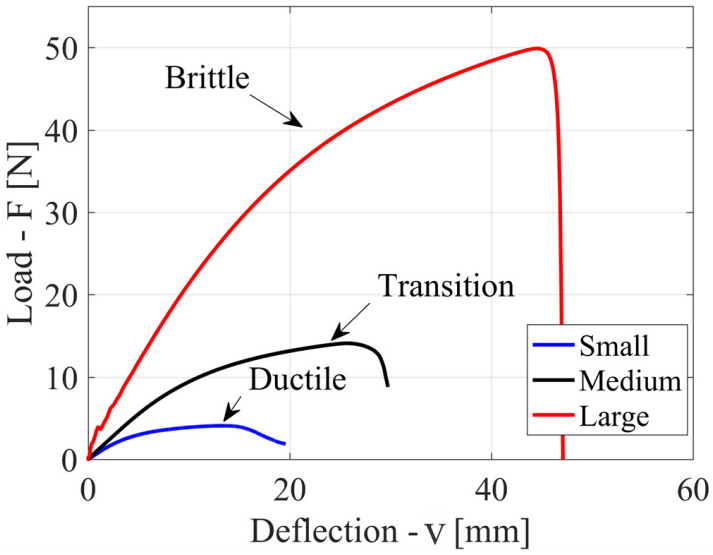


Figure 7. Numerical load–deflection curves in order to show the ductile-to-brittle transition behavior based on the stress brittleness number.

It is worth noting that the PD approach employed in this work considers the horizon as a material property, δ', such as a specifically critical crack length, as well as presented in Section 2.2. Therefore, by assuming R = 1.0 in Equation (22) and exploiting the stress brittleness number concept, the global behavior can be predicted by comparing the horizon material property value with the structural size, b. This exemplifies one of the great capabilities of the bilinear PD model proposed by Cabral et al. [43] and Friedrich et al. [46]. More precisely, with δ' equal to 40 mm and b the depth of the beam (see Table 1), then:

- It can be observed that only the L beam is capable of containing an internal crack of such a size, indicating an unstable crack propagation;
- On the other hand, the S beam size, cannot have an internal critical crack size (δ') equal to 40 mm, and therefore an unstable crack propagation is not allowed, being a ductile fracture behavior reported;
- Finally, since the M beam size has a characteristic size close to δ', a transitional behavior is reported.

Assuming that n_f^{PD} is equal to n_f (see the values presented above), the value of δ', by using Equation (22), is equal to 67 mm, 70 mm, and 82 mm for the S, M, and L samples, respectively. Consequently, a value of the same order is found by this approach when compared with that obtained by Equation (17).

Figure 8 shows the kinetic, elastic, and damage energies normalized with respect to the maximum elastic energy against the normalized time (being the normalized time equal to 1.0 corresponding to the end of the simulation) for each beam size obtained numerically and presented in Figure 6. It can be observed that the ratio between elastic and damage energy decreases when the ductile-to-brittle transition occurs. In fact, the L beam size is the only one that records a peak of kinetic energy at the moment of rupture, indicating an unstable crack propagation.

Figure 9 shows the fracture configuration for both the experimental and numerical L samples. For the numerical model, Figure 9b shows only the material particles with a damage index greater than 0.25. In both cases, the main crack starts in the lower central region and propagates vertically up to the upper part. The numerical results are in good agreement with experimental fracture configuration.

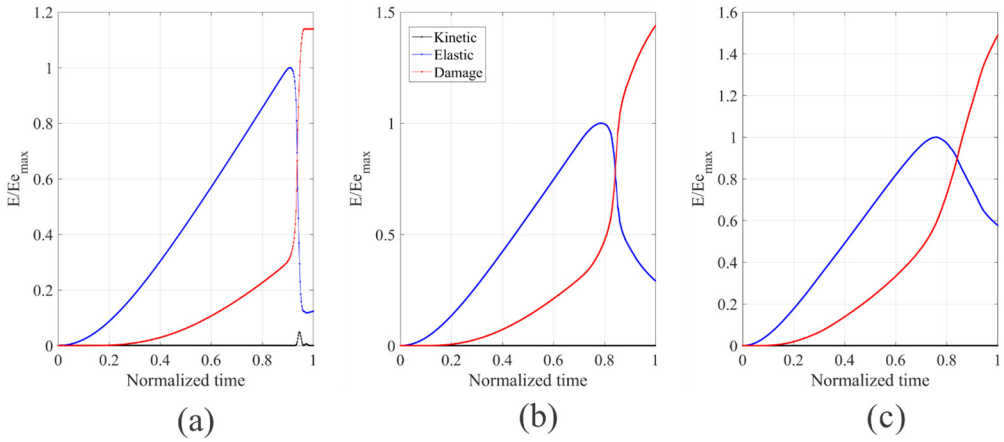


Figure 8. Kinetic, elastic, and damaged energies normalized with respect to the maximum elastic energy against the normalized time for: (**a**) L, (**b**) M, and (**c**) S sizes.

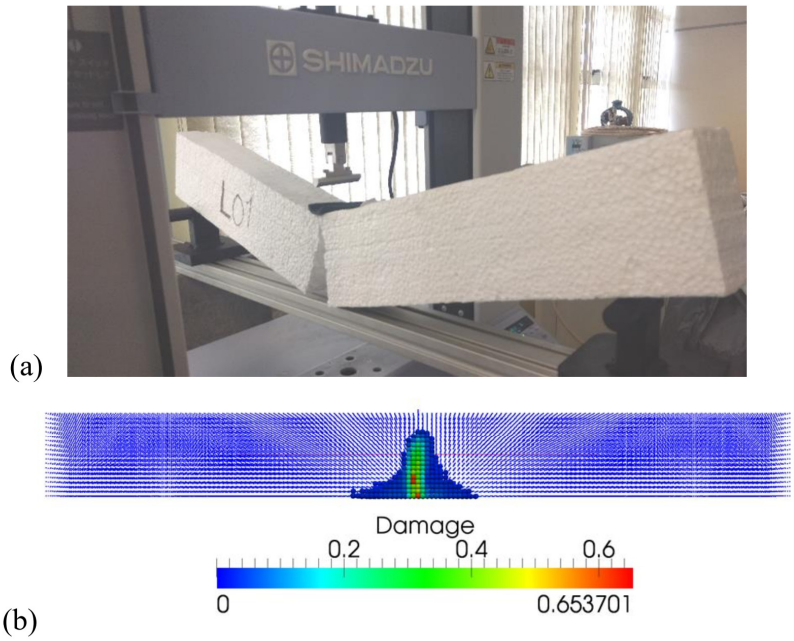


Figure 9. Final fracture configuration for the *L* beam size: (**a**) experimental and (**b**) numerical.

Figure 10 shows the experimental fracture surface observed for each one of the beam sizes under analysis. It can be observed that in the case of the *S* samples, which exhibited ductile fracture, a kind of transgranular fracture is evident, where only the grains had become detached from each other. In contrast, the *L* sample exhibits intergranular fractures in some regions of the cross-sectional area.

Details in Figure 10 show one of these regions, with the cut grains indicated by the red arrows. At these locations, the grains have been fractured, suggesting a link of this failure mechanism with the brittle fracture mode. These different failure mechanisms can be investigated through the application of various techniques, including Acoustic Emission (AE) [68,69]. Such a technique enables the identification of different sources, including cracks in opening mode (mode I) and shear mode (mode II) in concrete [70], as well as the fracture of fibers and matrix in composite materials [71].

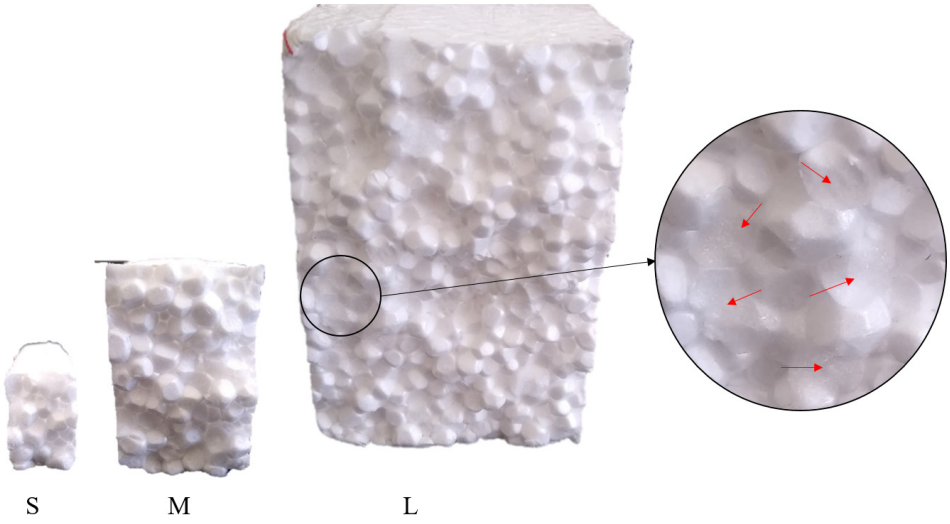


Figure 10. Fracture surface of the experimental samples S, M, and L, together with details of the intergranular failure mechanism (indicated by the red arrows).

4.2. Size Effect

Fractal Exponents

The fractal approach is one of the most widely used approaches to determine how material properties of quasi-brittle or disordered materials vary with scale. According to Lacidogna et al. [21], three mechanical properties can be evaluated from three-point bending tests: flexural strength, fracture energy, and angle of rotation. The measure of the variation of such properties with respect to their scale is determined by the so-called fractal exponents. In the following, these exponents are computed to the above properties and the experimental and numerical results are compared.

In Figure 11, the flexural strength vs. specimen size (beam depth-b) corresponding to the average value of each size (see Table 1) are presented in a bi-logarithm plot for the experimental and PD results. The scaling law is given by:

$$\ln \sigma = \ln \sigma^* - d_\sigma \ln b \tag{23}$$

where σ^* is the fractal flexural strength, which is a scale invariant material property. Thus, according to Figure 11, there is a flexural strength exponent $d_\sigma^{\text{exp}} = 0.098$ for the experimental results and $d_\sigma^{\text{Num}} = 0.129$ for the numerical simulations. This results in a fractal domain ($\Delta\sigma = 2 - d_\sigma$) that is equal to $\Delta\sigma_{\text{Exp}} = 1.902$ for the experiments and $\Delta\sigma_{\text{Num}} = 1.871$ for the PD simulations.

The fractal domain indicates that the flexural strength occurs over a ligament area smaller than a surface due to the presence of material defects. In the case of EPS, it can represent the voids between the spheres that make up the material. The influence of the heterogeneity of the material tends to decrease as the beam becomes increasingly larger. From a fractal point of view, lacunar sets can be associated with this type of result, such as the Cantor set [10].

To find the scale effect on the fracture energy, G_f, firstly the dissipated energy (W) should be computed. According to [21], it is defined by considering the area of the $F - \text{v}$ diagram, as shown in Figure 12. Due to the uncontrolled post peak behavior in both experimental test and numerical simulations, the area considered is that up to the peak load.

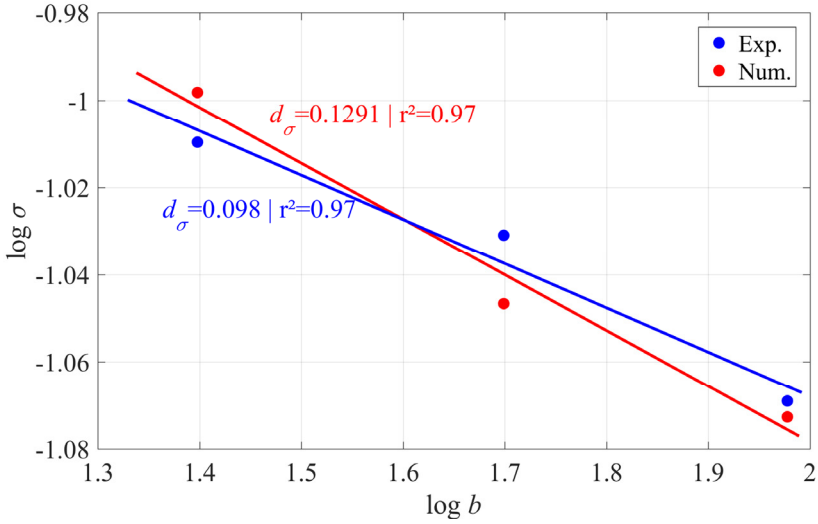


Figure 11. Bending strength vs. beam size diagram (*r* is Pearson correlation coefficient).

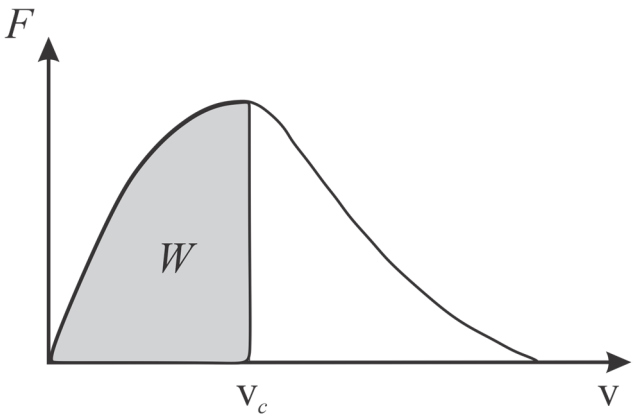


Figure 12. Load versus deflection to provide dissipated energy (*W*).

Table 4 shows the average values of the dissipated energy for the experimental and numerical results, together with its standard deviation. The error of the numerical results with respect to the experimental ones are presented as well. It can be observed that the sample size *M* presents the largest error when comparing the numerical results in relation to the experimental results. The greatest dispersion of results is observed for beams of size *S*, as can be seen from the standard deviation of these samples, both experimental and numerical.

Table 4. Dissipated energy (*W* in [J]) for experimental and numerical results.

Dissipated Energy [J]	S	M	L
Exp.	0.0466 ± 0.0062	0.293 ± 0.0098	1.590 ± 172.35
Num.	0.041 ± 0.0017	0.246 ± 0.0032	1.475 ± 16.81
Error	12.01%	16.04%	7.23%

The fracture energy is computed as the ratio of the dissipated energy by the cross-section beam area, *A*, that is $G_f = W/A$. It is worth mentioning that in both the work of Colpo et al. [72] and Kosteski et al. [73], where simulations based on the Lattice Discrete Element Method were performed, an energy balance method was employed as an alternative to calculate the G_f value. More precisely, taking into account the recorded energies (damage, elastic, and kinetic) involved in the fracture process, as presented, for example, in Figure 8

for PD simulations, different considerations were evaluated to identify the best way to calculate the fracture energy and its relationship with samples of different sizes.

The corresponding fractal scaling law is presented in Figure 13 by plotting the fracture energy vs. beam size (beam depth-b) on a bi-logarithmic scale:

$$\ln G_f = \ln G_f^* - d_G \ln b \tag{24}$$

where G_f^* is the fractal fracture energy, which is a scale invariant material property. Figure 13 shows $d_G^{\text{exp}} = 0.546$ and a fractal dimension ($\Delta G = 2 + d_G$) $\Delta G_{\text{Exp}} = 2.546$ for experimental results and $d_G^{\text{Num}} = 0.587$ with a fractal dimension equal to $\Delta G_{\text{Num}} = 2.587$. The d_G exponents show that energy is dissipated over a region larger than a surface, which can be described, from a fractal point of view, by invasive fractal sets, such as the von Koch triadic curve, for example.

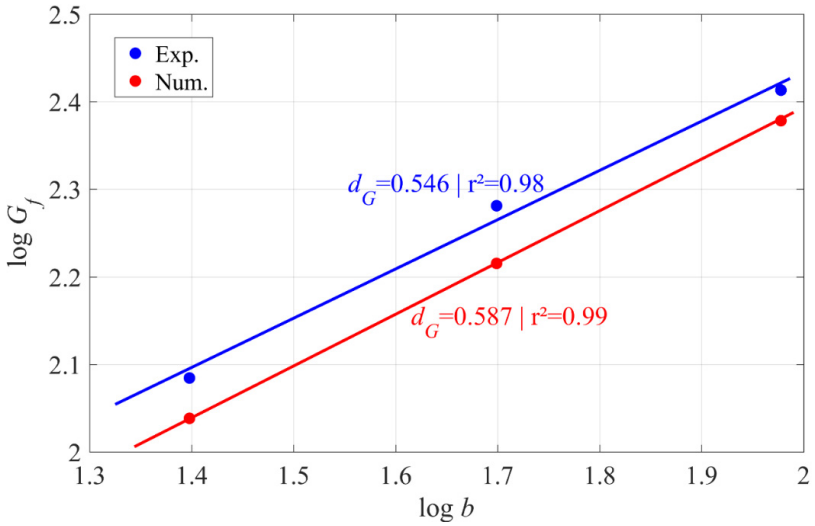


Figure 13. Fracture energy vs. beam size diagram (r is Pearson correlation coefficient).

In three-point bending tests, the fractal kinematic parameter considered, which has the same meaning as the critical displacement in a tensile test, is the localized rotation at the beam midspan. This parameter, at the point of view of failure, is defined as (see the variables in Figure 14):

$$\phi_c = \frac{v_c}{l/2} \tag{25}$$

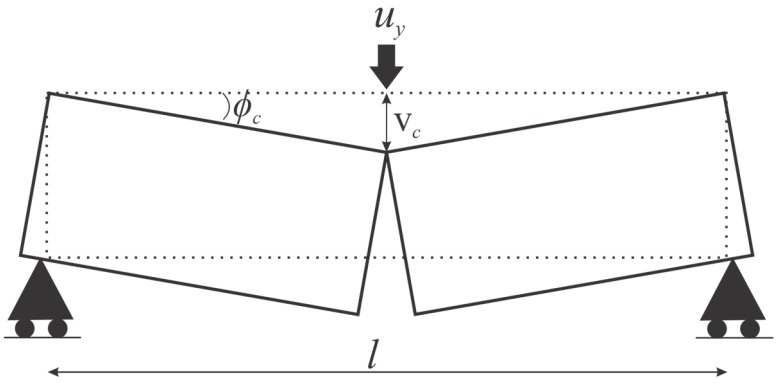


Figure 14. Parameters involved in critical rotation angle.

The corresponding fractal scaling law of the critical rotation angle on a bi-logarithmic scale is given by:

$$\ln \phi_c = \ln \phi_c^* - d\chi \ln b \tag{26}$$

where ϕ_c^* is the fractal critical rotation angle (invariant material property) and $d\chi$ is the fractal exponent of the rotation angle. Figure 15 shows for the experimental tests an exponent of $d_\chi^{\text{Exp}} = 0.343$ and for PD one of $d_\chi^{\text{Num}} = 0.269$. Carpinteri and Accornero [20] explain that the kinematic parameter is between the dimension of the rotation angle $[L]^0$ and a curvature $[L]^1$, that is, the parameter moves from a generalized displacement to a deformation. From the fractal point of view, the decrease in the kinematic parameter represents the curvature, located in the beam span, as a lacunar fractal consisting of infinite radial cracks converging to the center of curvature.

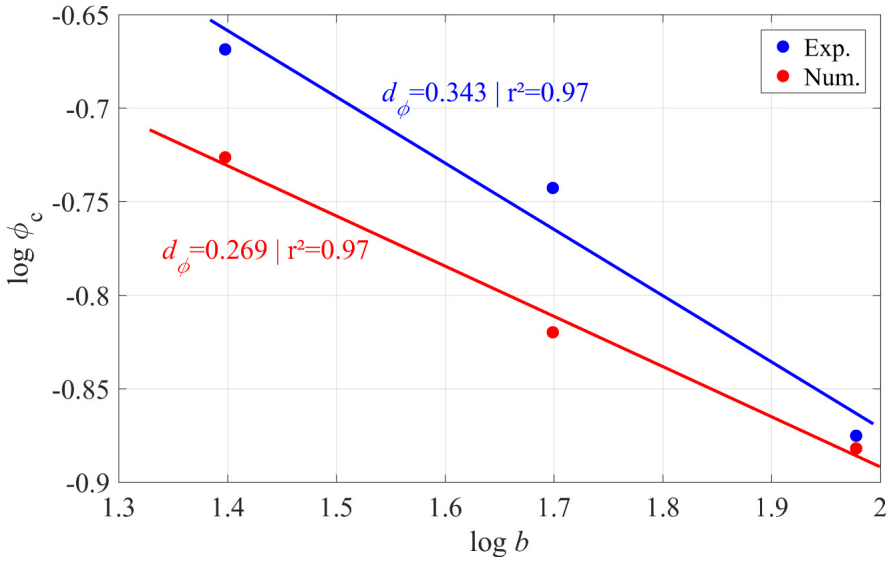


Figure 15. Critical rotation vs. beam size diagram (r is Pearson correlation coefficient).

Finally, according to the fractal size effect law, presented by Carpinteri and colleagues [7], the fundamental relationship between the fractal exponents is defined by:

$$d\sigma + d\chi + dG = 1 \tag{27}$$

In the context of this work, the experimental tests provide for Equation (27) a value of 0.988, whereas the numerical results provide a value equal to 0.979, that is, an error, computed with respected to the theoretical one, equal to -1.20% and -2.10%, respectively. Therefore it is clear that the experimental and numerical results are in agreement with the fractal approach of the size effect.

It is worth noting that in previous studies carried out by some of the authors of this work, using a version of the Discrete Element Method (DEM) [73,74], it was demonstrated that the scale effect in quasi-brittle materials can be obtained by considering a bilinear relationship together with the implementation of random fields. The same approach has also been used in the PD simulations presented in this work, again demonstrating its effectiveness in capturing the scale effect. In both cases (DEM and PD simulations) the results are consistent with those predicted by the fractal size effect theory.

The numerical results obtained in this work on the scale effect in quasi-brittle materials are of great importance for researchers whose work is based on PD theory, since it has received unfair criticism, such as those presented by Bazant et al. [49]. Based on the findings of this work, it will be possible to extend the studies to increasingly larger scales with the

use of new parallel programming techniques and software, thus assisting engineers in the design of new structures.

4.3. Dimensional Analysis for the Size Effect Based on the BPD Model Parameters

The scale effect presented above reflects the dependence of some mechanical quantities on a small range of scales, more precisely, the laboratory scale. However, when the scales are particularly small or large, a power relationship between the mechanical quantity and size is no longer observed. Based on this, the classical dimensional analysis is employed to demonstrate that the scale effect is naturally described by the parameters of the BPD model.

According to Zohuri [75], the dimensional analysis is a method by which information about a phenomenon is derived from the single premise that a phenomenon can be described by a dimensionally consistent equation of certain variables. As described by Barenblatt [76], the functional relationship between a studied quantity and its governing parameters can be expressed using the following equation:

$$a = F(a_1, \ldots, a_k, b_1, \ldots, b_m) \tag{28}$$

where a is the quantity being determined in the study, $a_{1:k}$ represent the governing parameters with independent physical dimensions, $b_{1:m}$ represent the governing parameters with dependent dimensions, that is, their dimensions can be written in terms of the dimensions of the parameters $a_{1:k}$, and F is the function which represents the functional relationship that exists between the parameters and the quantity studied. In the context of physical phenomena in mechanics, the physical quantities are typically represented in the MLT system, that is mass, length, and time. In this case, the independent physical dimensions are three, which implies $k = 3$. The theorem of groups $\prod$, originally presented by Buckingham in 1914 [77], allows for the expression (28) to be presented in an alternative form as:

$$\prod = \Phi\left(\prod_1, \ldots, \prod_m\right) \tag{29}$$

with

$$\Pi = \frac{a}{a_1^p \ldots a_k^r} \text{ and } \Pi_{i=1:m} = \frac{b_i}{a_1^{p_i} \ldots a_k^{r_i}} \tag{30}$$

where the exponents (p and r) of the governing parameters with independent dimensions are chosen such that all the parameters $\prod$, and $\prod_{1:m}$ are dimensionless. The function Φ represents the functional relationship that exists between these dimensionless parameters.

According to Barenblatt [76], these results lead to the central theorem in dimensional analysis, the so-called $\prod$-theorem: a physical relationship between some dimensional (generally speaking) quantity and several dimensional governing parameters can be rewritten as a relationship between a dimensionless parameter and several dimensionless products of the governing parameters; the number of dimensionless products is equal to the total number of governing parameters minus the number of governing parameters with independent dimensions. The term 'physical relationship' is used to emphasize that it should be valid in all systems of units.

Barenblat [76] shows that expression (29) can be written as follows:

$$\Pi = C\ (\Pi_1)^{\alpha_1} (\Pi_2)^{\alpha_2} \ldots\ldots (\Pi_m)^{\alpha_m} \tag{31}$$

where C and $\alpha_{1:m}$ are coefficients that must be determined depending on the specific case analyzed. In Refs. [75,76], different technics have been proposed in order to reduce the number of dimensionless parameters or to determine the coefficients $\alpha_{1:m}$.

Taking into account the BPD model parameters, an analysis of the mechanical properties affected by the scale effect will be conducted using the dimensional analysis. This analysis can be done for the case of three-point bending tests; however, for simplicity, we will consider a plate with dimensions *bxb* and thickness *e* under tension. Therefore, the size effect on the tensile strength (σ_u), the fracture energy available to break the specimen when σ_u is reached (G_f), and the ultimate strain (ε_u), which corresponds to σ_u, will be examined.

By considering the MLT system (then $k = 3$), the following govern model parameters are defined: young modulus, E (a_1), the characteristic plate dimension, b (a_2), and the material density, ρ (a_3). The dependent model parameters are assumed as: $\overline{G}_f, \delta', CV_{Gf}, L_{corr}$. $\overline{G}_f$ is an input data; a measure of the fracture energy, independent of the body size, linked with the energy below the bilinear relationship.

Equation (28) for σ_u, G_f, and ε_u could be expressed as:

$$\sigma_u = \mathbf{X}(a_1, a_2, a_3, b_1, b_2, b_3, b_4) = \mathbf{X}(E, b, \rho, \overline{G}_f, \delta', CV_{Gf}, L_{corr}) \tag{32}$$

$$G_f = \mathbf{Y}(a_1, a_2, a_3, b_1, b_2, b_3, b_4) = \mathbf{Y}(E, b, \rho, \overline{G}_f, \delta', CV_{Gf}, L_{corr}) \tag{33}$$

$$\varepsilon_u = \mathbf{Z}(a_1, a_2, a_3, b_1, b_2, b_3, b_4) = \mathbf{Z}(E, b, \rho, \overline{G}_f, \delta', CV_{Gf}, L_{corr}) \tag{34}$$

By employing the technique of dimensional analysis, the $\prod$ terms can be written as follows:

$$\Pi_{\sigma u} = \Phi_{\sigma u}(\Pi_1, \Pi_2, \Pi_3, \Pi_4) = C_{\sigma u}(\Pi_1)^{\alpha_1}(\Pi_2)^{\alpha_2}(\Pi_3)^{\alpha_3}(\Pi_4)^{\alpha_4} \tag{35}$$

$$\Pi_{Gf} = \Phi_{Gf}(\Pi_1, \Pi_2, \Pi_3, \Pi_4) = C_{Gf}(\Pi_1)^{\beta_1}(\Pi_2)^{\beta_2}(\Pi_3)^{\beta_3}(\Pi_4)^{\beta_4} \tag{36}$$

$$\Pi_{\varepsilon u} = \Phi_{\varepsilon u}(\Pi_1, \Pi_2, \Pi_3, \Pi_4) = C_{\varepsilon u}(\Pi_1)^{\gamma_1}(\Pi_2)^{\gamma_2}(\Pi_3)^{\gamma_3}(\Pi_4)^{\gamma_4} \tag{37}$$

where,

$$\begin{aligned} \Pi_{\sigma u} &= \sigma_u/(E^1 b^0 \rho^0) = \sigma_u/E \\ \Pi_{Gf} &= G_f/(E^1 b^1 \rho^0) = G_f/(Eb) \\ \Pi_{\varepsilon u} &= \varepsilon_u/(E^0 b^0 \rho^0) = \varepsilon_u \end{aligned} \tag{38}$$

From Equations (35)–(37), it's possible to write:

$$\Pi_1 = \overline{G}_f/(E^1 b^1 \rho^0) = \overline{G}_f/(E\, b) \tag{39}$$

$$\Pi_2 = \delta'/(E^0 b^1 \rho^0) = \delta'/b \tag{40}$$

$$\Pi_3 = CV_{Gf}/(E^0 b^0 \rho^0) = CV_{Gf} \tag{41}$$

$$\Pi_4 = L_{corr}/(E^0 b^1 \rho^0) = L_{corr}/b \tag{42}$$

In this preliminary study, the analysis will be limited to the interaction between the size effect and the parameters $\prod_1$ and $\prod_2$. The dimensionless variables $\prod_3$ and $\prod_4$ will not be addressed at this stage, as they are not the focus of this investigation.

By rewriting the expression (35)–(37), and combining them with (39) and (40), it is possible to obtain:

$$\sigma_u/E = C_{\sigma u}\left(\overline{G}_f/(E\, b)\right)^{\alpha_1}(\delta'/b)^{\alpha_2} \tag{43}$$

$$G_f/(E\, b) = C_{Gf}(\overline{G}_f/(E\, b)^{\beta_1}(\delta'/b)^{\beta_2} \tag{44}$$

$$\varepsilon_u = C_{\varepsilon u}(\overline{G}_f/(E\, b))^{\gamma_1}(\delta'/b)^{\gamma_2} \tag{45}$$

The next step is to perform dimensional analysis for each of the mechanical quantities affected by scale under tension for samples that exhibit a tendency towards a small scale

(when $b \to 0$), as well as those that show a tendency towards larger structures (when $b \to \infty$). For simplicity let us assume in the following that $\overline{G}_f = G_f$.

For the tensile strength, the expression (43) is rewritten as follows:

$$\sigma_u = C_{\sigma u} E \left(\overline{G}_f / (E\, b) \right)^{\alpha_1} (\delta' / b)^{\alpha_2} \tag{46}$$

By considering $\alpha_1 = 0.5$ for all the structural sizes (b), the following analisys can be perfomed in order to defined the size effect on the tensile strength:

- when $b \to 0$, assuming $\alpha_2 = -0.5$ and considering Equation (12) with $R = 1.0$, Equation (46) becomes:

$$\sigma_u = C_{\sigma u} E \left(\overline{G}_f / (E\, b) \right)^{0.5} (\delta' / b)^{-0.5} \tag{47a}$$

$$\sigma_u = C_{\sigma u} E \left(\overline{G}_f / (E\, \delta') \right)^{0.5} \tag{47b}$$

$$\sigma_u = C_{\sigma u} E s' \tag{47c}$$

$$\sigma_u \propto b^{0.0} \tag{47d}$$

- when $b \to \infty$, assuming $\alpha_2 = 0.0$ and considering Equation (12) with $R = 1.0$, Equation (46) becomes:

$$\sigma_u = C_{\sigma u} E \left(\overline{G}_f / (E\, b) \right)^{0.5} (\delta' / b)^{0.0} \tag{48a}$$

$$\sigma_u = C_{\sigma u} E \left(\overline{G}_f / (Eb) \right)^{0.5} (\delta' / \delta')^{0.5} \tag{48b}$$

$$\sigma_u = C_{\sigma u} E s' (\delta' / b)^{0.5} \tag{48c}$$

$$\sigma_u \propto b^{-0.5} \tag{48d}$$

Therefore, the dimensional analysis returns the trend presented in Figure 16a for the size effect for the tensile strength.

It should be noted that the relationship presented in Equation (48a) can also be rearranged as follows:

$$\sigma_u = C_{\sigma u} (G_f E / b)^{0.5} = C_{\sigma u} K_{IC} / b^{0.5} \;\; \therefore \frac{K_{IC}}{b^{0.5}} \propto \frac{K_{IC}}{(\pi a)^{0.5}} \tag{49}$$

Therefore, for large structures, the tensile strength scaling law follows the LEFM.

The trends of the tensile strength scaling law (Figure 16a) indicates that for smaller samples, a homogeneous regime should be assumed, where there is no variation of the strength with respect to the dimensions of the sample ($d\sigma_u = 0.0$). On the other hand, for larger samples, it is evident that the tensile strength is governed by the LEFM (see Equation (49)), resulting in a scaling exponent ($d\sigma_u$) equal to 0.5.

By considering in Equation (44) β_1 equal to 1.0 for all the structural sizes (b), the following analysis can be performed in order to defined the size effect on the fracture energy:

- when $b \to 0$, assuming $\beta_2 = -1.0$,

$$G_f = E\, b C_{Gf} (\overline{G}_f / (E\, b))^1 (\delta' / b)^{-1} \tag{50a}$$

$$G_f = E\, bC_{Gf}(\overline{G}_f/(E\,\delta')) \tag{50b}$$

$$G_f = C_{Gf} bEs'^2 \tag{50c}$$

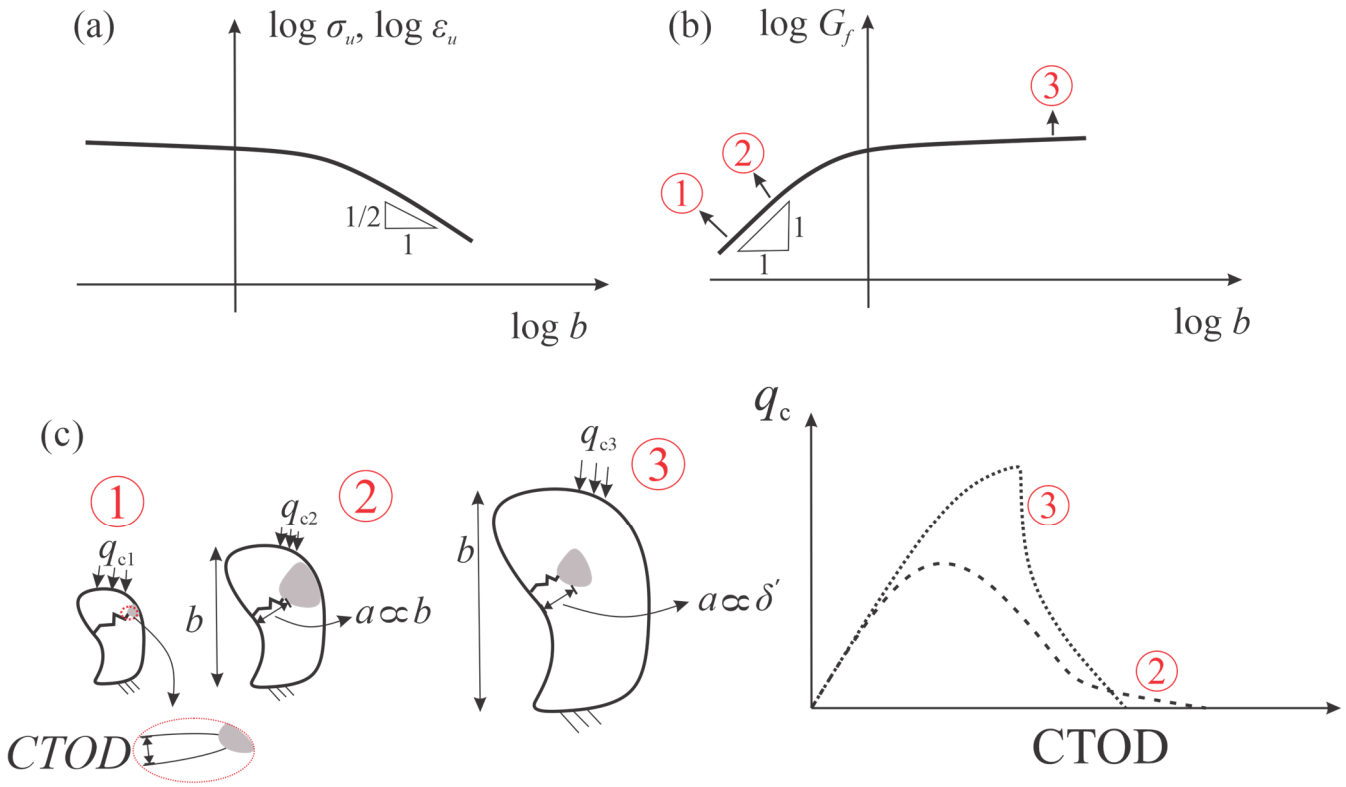


Figure 16. Scaling laws derived from dimensional analysis of BPD model parameters. (**a**) Tensile strength and critical strain and (**b**) fracture energy. (**c**) Schematic representation of fracture energy scaling law. In (**b**,**c**) the numbers 1 to 3 indicate the characteristic dimension, b, of scaled similar structures.

By remembering the relationship between the Crack Tip Opening Displacement (*CTOD*) [78] and G_f (that is, $G_f = \sigma_u CTOD$) and assuming in Equation (50c), Es' a stress at failure, σ_u, then the CTOD, and consequently G_f, is proportional to $s'b$, that is,

$$G_f \propto b^{1.0} \tag{50d}$$

- when $b \to \infty$ and assuming $\beta_2 = 0.0$,

$$G_f = E\, bC_{Gf}(\overline{G}_f/(E\,b))^1(\delta'/b)^0 \tag{51a}$$

$$G_f = E\, bC_{Gf}(\overline{G}_f/(E\,b))^1(\delta'/\delta')^1 \tag{51b}$$

$$G_f = E\, C_{Gf}(\overline{G}_f/(E\,\delta'))^1\delta' \tag{51c}$$

$$G_f = E\, C_{Gf}s'^2\delta' \tag{51d}$$

By recalling the G_f and CTOD relationship presented above, and combining it with Equation (12), being $R = 1.0$ and $\sigma_u = Es'$ in Equation (51d), then the CTOD and consequently G_f, is proportional to $s'\delta'$, that is,

$$G_f \propto b^{0.0} \tag{51e}$$

Equations (50d) and (51e) return the trend present in Figure 16b for the fracture energy scaling law. Figure 16c shows a schematic representation of the fracture energy scaling law, taking into account different body sizes, b, under a given boundary condition and loading (q_c). The representation of the CTOD is presented as well. More precisely, for samples of a relatively small size, the CTOD value is proportional to the sample size, b ($dG_f = 1.0$). This means that for any small body with a crack (which will appear at the moment of fracture), the CTOD, and consequently the critical crack size, is restricted to size of the sample. On the other hand, for large samples, the CTOD, and consequently the critical crack size, are governed by δ', and therefore constant, that is $dG_f = 0.0$ (see Figure 16b).

Finally, by considering in Equation (45) γ_1 equal to 0.5 for all the structural sizes (b), the following analysis can be performed in order to defined the size effect on the critical strain:

- when $b \to 0$, assuming $\gamma_2 = -0.5$ and considering Equation (12) with $R = 1.0$,

$$\varepsilon_u = C_{\varepsilon u}(\overline{G}_f/(E\,b))^{0.5}(\delta'/b)^{-0.5} \tag{52a}$$

$$\varepsilon_u = C_{\varepsilon u}(\overline{G}_f/(E\,\delta'))^{0.5} \tag{52b}$$

$$\varepsilon_u = C_{\varepsilon u}s' \tag{52c}$$

$$\varepsilon_u \propto b^{0.0} \tag{52d}$$

- when $b \to \infty$, assuming $\gamma_2 = 0.0$ and considering Equation (12) with $R = 1.0$,

$$\varepsilon_u = C_{\varepsilon u}(\overline{G}_f/(E\,b))^{0.5}(\delta'/b)^{0.0} \tag{53a}$$

$$\varepsilon_u = C_{\varepsilon u}(\overline{G}_f/(E\,b))^{0.5}(\delta'/\delta')^{0.5} \tag{53b}$$

$$\varepsilon_u = C_{\varepsilon u}s'(\delta'/b)^{0.5} \tag{53c}$$

$$\varepsilon_u \propto b^{-0.5} \tag{53d}$$

Therefore, dimensional analysis returns for the critical strain scaling law trend are presented in Figure 16a. When $b \to 0$, a homogeneous regime is expected (exactly as in tensile strength), the strains being diffuse, that is, occurring throughout the volume of the body. Consequently, there is no scale effect on the critical strain, $d\varepsilon_u = 0.0$. When $b \to \infty$, the strain will be in accordance with the behavior of the tensile strength up to the peak stress, which is governed by the LEFM. Consequently, the scale effect will follow the same trend, that is, $d\varepsilon_u = 0.5$.

It is worth noting that the sum of three fractal exponents will be equal to 1.0 from the scaling laws derived from dimensional analysis employing the BPD model parameters.

5. Conclusions

In the present work, the problem of size effect is analyzed from a fractal point of view in EPS beam specimens subjected to three-point bending tests and PD simulations. More specifically, three scaled beams are considered and the size effect on flexural strength, fracture energy and critical angle of rotation is investigated.

It was found from the global behavior analysis that the maximum absolute errors, calculated with respect to the experimental values, are:

- On average, flexural strength equal to 3.54%;
- On average, flexural strain equal to 7.14%;
- On average, dissipated energy equal to 16.04%.

Regarding the size effect analysis, the sum of the fractal exponents shows an error, calculated with respect to the theoretical one, equal to -1.20% and -2.10% for the experimental and numerical results, respectively. Moreover, the ductile-to-brittle transition behavior is observed in both experimental and numerical results, a clear signature of the size effect in quasi-brittle materials.

By employing the classical dimensional analysis, the size effect on the mechanical properties of quasi-brittle materials based on the parameters that govern the BPD model has been investigated. The results showed that the trends reported by dimensional analysis, allowing the extrapolation of the results obtained from the BPD model to different scales in addition to the laboratory ones analyzed in the work. More precisely, the results of dimensional analysis show that:

- For the tensile strength and the critical strain, the same trends are observed, that is, when $b \to 0$, no scale effect is reported, whereas when $b \to \infty$, these mechanical properties are governed by the LEFM;
- For the fracture energy, when $b \to 0$, the size dependence is maximum, that is, directly proportional to the structural size, whereas when $b \to \infty$, no scale effect is observed.

Future research work will examine the scale effect across a broader range of sizes than those considered in this study. This will be achieved by implementing advanced parallelization techniques to optimize computational time. Additionally, the analysis will include the influence of quasi-brittle materials under different loading conditions, such as, for example, traction and compression.

Author Contributions: Conceptualization, L.F.F., É.S.C., I.I., G.L., and C.B.; Methodology, L.F.F., L.E.K., É.S.C., and C.B.; Formal analysis, L.F.F.; Investigation, L.F.F., A.B.C., and É.S.C.; Writing—original draft preparation, L.F.F. and É.S.C.; Writing—review and editing, L.E.K., I.I., and G.L.; Visualization, L.F.F. and A.B.C.; Supervision, L.F.F., I.I., and G.L. All authors have read and agreed to the published version of the manuscript.

Funding: This research received no funding.

Data Availability Statement: Data will be made available on request.

Acknowledgments: The authors wish to acknowledge the Brazilian National Council for Scientific and Technological Development (CNPq) and the Coordination for the Improvement of Higher Level of Education Personnel (CAPES).

Conflicts of Interest: The authors declare no conflicts of interest.

References

1. Carpinteri, A.; Chiaia, B. Multifractal scaling laws in the breaking behaviour of disordered materials. *Chaos Solitons Fract.* **1997**, *8*, 135–150. [CrossRef]
2. Borst, R. Fracture and damage in quasi-brittle materials: A comparison of approaches. *Theor. Appl. Fract. Mech.* **2022**, *122*, 103652. [CrossRef]

3. Berto, F.; Lazzarin, P. Recent developments in brittle and quasi-brittle failure assessment of engineering materials by means of local approaches. *Mater. Sci. Eng. R Rep.* **2014**, *75*, 1–48. [CrossRef]
4. Bazant, Z.P. Scaling of quasibrittle fracture: Asymptotic analysis. *Int. J. Fract.* **1997**, *83*, 19–40. [CrossRef]
5. Bazant, Z.P. Scaling theory for quasibrittle structural failure. *Proc. Natl. Acad. Sci. USA* **2004**, *101*, 13400–13407. [CrossRef]
6. Bažant, Z.P. Design of quasibrittle materials and structures to optimize strength and scaling at probability tail: An apercu. *Proc. R. Soc. A* **2019**, *475*, 20180617. [CrossRef]
7. Carpinteri, A. Fractal nature of material microstructure and size effects on apparent mechanical properties. *Mech. Mater.* **1994**, *18*, 89–101. [CrossRef]
8. Carpinteri, A.; Chiaia, B. Multifractal nature of concrete fracture surfaces and size effects on nominal fracture energy. *Mater. Struct.* **1995**, *28*, 435–443. [CrossRef]
9. Carpinteri, A.; Ciola, F.; Pugno, N. Boundary element method for the strain-softening response of quasi-brittle materials in compression. *Comput. Struct.* **2001**, *79*, 389–401. [CrossRef]
10. Carpinteri, A.; Chiaia, B.; Cornetti, P. A scale-invariant cohesive crack model for quasi-brittle materials. *Eng. Fract. Mech.* **2002**, *69*, 207–217. [CrossRef]
11. Rinaldi, A.; Mastilovic, S. The Krajcinovic approach to model size dependent fracture in quasi-brittle solids. *Mech. Mater.* **2014**, *71*, 21–33. [CrossRef]
12. Mandelbrot, B.; Passoja, D.; Paullay, A. Fractal character of fracture surfaces of metals. *Nature* **1984**, *308*, 721–722. [CrossRef]
13. Carpinteri, A.; Puzzi, S. The fractal-statistical approach to the size-scale effects on material strength and toughness. *Probabilist. Eng. Mech.* **2009**, *24*, 75–83. [CrossRef]
14. Borodich, F.M. Fractals and fractal scaling in fracture mechanics. *Int. J. Fract.* **1999**, *95*, 239–259. [CrossRef]
15. van Vliet, M.R.A.; van Mier, J.G.M. Experimental investigation of size effect in concrete and sandstone under uniaxial tension. *Eng. Fract. Mech.* **2000**, *65*, 165–188. [CrossRef]
16. Carpinteri, A. Scaling laws and renormalization groups for strength and toughness of disordered materials. *Int. J. Solids Struct.* **1994**, *31*, 291–302. [CrossRef]
17. Carpinteri, A. Strength and toughness in disordered materials: Complete and incomplete similarity. In *Size-Scale Effects in the Failure Mechanisms of Materials and Structures*; CRC Press: Boca Raton, FL, USA, 2002; pp. 17–40. [CrossRef]
18. Carpinteri, A.; Ferro, G. Size effects on tensile fracture properties: A unified explanation based on disorder and fractality of concrete microstructure. *Mater. Struct.* **1994**, *27*, 563–571. [CrossRef]
19. Carpinteri, A.; Ferro, G. Scaling behaviour and dual renormalization of experimental tensile softening responses. *Mater. Struct.* **1998**, *31*, 303–309. [CrossRef]
20. Carpinteri, A.; Accornero, F. Rotation Versus Curvature Fractal Scaling in Bending Failure. *Phys. Mesomech.* **2019**, *22*, 46–51. [CrossRef]
21. Lacidogna, G.; Piana, G.; Accornero, F.; Carpinteri, A. Multi-technique damage monitoring of concrete beams: Acoustic Emission, Digital Image Correlation, Dynamic Identification. *Constr. Build. Mater.* **2020**, *242*, 118114. [CrossRef]
22. Carpinteri, A.; Ciola, F.; Pugno, N.; Ferrara, G.; Gobbi, M.E. Size-scale and slenderness influence on the compressive strain-softening behaviour of concrete. *Fatigue Fract. Eng. Mater. Struct.* **2001**, *24*, 441–450. [CrossRef]
23. Lei, W.-S.; Qian, G.; Yu, Z.; Berto, F. Statistical size scaling of compressive strength of quasi-brittle materials incorporating specimen length-to-diameter ratio effect. *Theor. Appl. Fract. Mech.* **2019**, *104*, 102345. [CrossRef]
24. Issa, M.A.; Issa, M.A.; Islam, S.; Chudnovsky, A. Size effects in concrete fracture: Part I, experimental setup and observations. *Int. J. Fract.* **2000**, *102*, 1–24. [CrossRef]
25. Mier, V.; Vliet, V. Uniaxial tension test for the determination of fracture parameters of concrete: A state of the art. *Eng. Fract. Mech.* **2002**, *69*, 235–247. [CrossRef]
26. Wright, P.J.F. The effect of the method of test on the flexural strength of concrete. *Mag. Concrete Res.* **1952**, *11*, 67–76. [CrossRef]
27. Bažant, Z.P.; Sun, H.H. Size effect in diagonal shear failure: Influence of aggregate size and stirrups. *ACI Mater. J.* **1987**, *84*, 259–272.
28. Zhou, F.P.; Balendran, R.V.; Jeary, A.P. Size effect on flexural, splitting tensile, and torsional strengths of high-strength concrete. *Cem. Concr. Res.* **1998**, *28*, 1725–1736. [CrossRef]
29. Barenblatt, G.I. The formation of equilibrium cracks during brittle fracture. General ideas and hypotheses. Axially symmetric cracks. *J. Appl. Math. Mech.* **1959**, *23*, 622–636.
30. Belytschko, T.; Black, T. Elastic crack growth in finite elements with minimal remeshing. *Int. J. Numer. Methods Eng.* **1999**, *45*, 601–620. [CrossRef]
31. Miehe, C.; Hofacker, M.; Welschinger, F. Phase field model for rate-independent crack propagation: Robust algorithmic implementation based on operator splits. *Comput. Methods Appl. Mech. Eng.* **2010**, *199*, 2765–2778. [CrossRef]
32. Cundall, P.A.; Strack, O.D. A discrete numerical model for granular assemblies. *Geotechnique* **1979**, *29*, 47–65. [CrossRef]

33. Rizvi, Z.H.; Shrestha, D.; Sattari, A.S.; Wuttke, F. Numerical modelling of effective thermal conductivity for modified geomaterial using lattice element method. *Heat Mass Transf.* **2018**, *54*, 483–499. [CrossRef]
34. Rios, J.D.; Riera, J.D. Size effects in the analysis of reinforced concrete structures. *Eng. Struct.* **2004**, *26*, 1115–1125. [CrossRef]
35. Cervera, M.; Barbat, G.B.; Chiumenti, M.; Wu, J.-Y. A comparative review of XFEM, Mixed FEM and Phase-Field models for quasi-brittle cracking. *Arch. Comput. Methods Eng.* **2022**, *29*, 1009–1083. [CrossRef]
36. Nikolić, M.; Karavelić, E.; Ibrahimbegovic, A. Lattice element models and their peculiarities. *Arch. Comput. Methods Eng.* **2018**, *25*, 753–784. [CrossRef]
37. Pathirage, M.; Tong, D.; Thierry, F.; Cusatis, G.; Grégoire, D.; Pijaudier-Cabot, G. Discrete modeling of concrete failure and size-effect. *Theor. Appl. Fract. Mech.* **2023**, *124*, 103738. [CrossRef]
38. Silling, S.A. Reformulation of elasticity theory for discontinuities and long-range forces. *J. Mech. Phys. Solids* **2000**, *48*, 175–209. [CrossRef]
39. Jenabidehkordi, A. Computational methods for fracture in rock: A review and recent advances. *Front. Struct. Civ. Eng.* **2019**, *13*, 273–287. [CrossRef]
40. Tong, Y.; Shen, W.; Shao, J.; Chen, J. A new bond model in peridynamics theory for progressive failure in cohesive brittle materials. *Eng. Frac. Mech.* **2020**, *223*, 106767. [CrossRef]
41. Isiet, M.; Miskovic, I.; Miskovic, S. Review of peridynamic modelling of material failure and damage due to impact. *Int. J. Impact Eng.* **2021**, *147*, 103740. [CrossRef]
42. Ni, T.; Zhu, Q.; Zhao, L.; Li, P. Peridynamic simulation of fracture in quasi-brittle solids using irregular finite element mesh. *Eng. Fract. Mech.* **2018**, *188*, 320–343. [CrossRef]
43. Cabral, N.R.; Invaldi, M.A.; D'Ambra, R.B.; Iturrioz, I. An alternative bilinear peridynamic model to simulate the damage process in quasi-brittle materials. *Eng. Fract. Mech.* **2019**, *216*, 106494. [CrossRef]
44. Yu, H.; Chen, X.; Sun, Y. A generalized bond-based peridynamic model for quasi-brittle materials enriched with bond tension–rotation–shear coupling effects. *Comput. Methods Appl. Mech. Eng.* **2020**, *372*, 113405. [CrossRef]
45. Li, S.; Lu, H.; Jin, Y.; Sun, P.; Huang, X.; Bie, Z. An improved unibond dual-parameter peridynamic model for fracture analysis of quasi-brittle materials. *Int. J. Mech. Sci.* **2021**, *204*, 106571. [CrossRef]
46. Friedrich, L.F.; Colpo, A.B.; Kosteski, L.E.; Vantadori, S.; Iturrioz, I. A novel peridynamic approach for fracture analysis of quasi-brittle materials. *Int. J. Mech. Sci.* **2022**, *227*, 107445. [CrossRef]
47. Friedrich, L.F.; Iturrioz, I.; Colpo, A.B.; Vantadori, S. Fracture failure of quasi-brittle materials by a novel peridynamic model. *Compos. Struct.* **2023**, *323*, 117402. [CrossRef]
48. Hobbs, M.; Dodwell, T.; Hattori, G.; Orr, J. An examination of the size effect in quasi-brittle materials using a bond-based peridynamic model. *Eng. Struct.* **2022**, *262*, 114207. [CrossRef]
49. Bažant, Z.P.; Nguyen, H.T.; Dönmez, A.A. Critical comparison of Phase-Field, Peridynamics, and Crack Band Model M7 in light of Gap Test and classical fracture tests. *J. Appl. Mech.* **2022**, *89*, 061008. [CrossRef]
50. Zhang, Y.; Deng, J.; Deng, H.; Ke, B. Peridynamics simulation of rock fracturing under liquid carbon dioxide blasting. *Int. J. Damage Mech.* **2019**, *28*, 1038–1052. [CrossRef]
51. Silling, S.A.; Askari, E. A meshfree method based on the peridynamic model of solid mechanics. *Comput. Struct.* **2005**, *83*, 1526–1535. [CrossRef]
52. Madenci, E.; Oterkus, E. *Peridynamic Theory and its Applications*; Springer: New York, NY, USA, 2014; pp. 45–145.
53. Taylor, D. *The Theory of Critical Distances: A New Perspective in Fracture Mechanics*; Elsevier Science: Amsterdam, The Netherlands, 2007.
54. Castro, J.; Cicero, S.; Sagaseta, C. A Criterion for Brittle Failure of Rocks Using the Theory of Critical Distances. *Rock Mech. Rock Eng.* **2016**, *49*, 63–77. [CrossRef]
55. Gerstle, W.; Sau, N.; Silling, S. Peridynamic modeling of concrete structures. *Nucl. Eng. Des.* **2007**, *237*, 1250–1258. [CrossRef]
56. Niazi, S.; Chen, Z.; Bobaru, F. Crack nucleation in brittle and quasi-brittle materials: A peridynamic analysis. *Theor. Appl. Fract. Mech.* **2021**, *112*, 103041. [CrossRef]
57. Sheikhbahaei, P.; Mossaiby, F.; Shojaei, A. An efficient peridynamic framework based on the arc-length method for fracture modeling of brittle and quasi-brittle problems with snapping instabilities. *Comput. Math. Appl.* **2023**, *136*, 165–190. [CrossRef]
58. Chen, Z.; Niazi, S.; Zhang, G.; Bobaru, F. Peridynamic functionally graded and porous materials: Modeling fracture and damage. In *Handbook of Nonlocal Continuum Mechanics for Materials and Structures*; Springer: Cham, Switzerland, 2017; pp. 1–35.
59. Chen, Z.; Niazi, S.; Bobaru, F. A peridynamic model for brittle damage and fracture in porous materials. *Int J. Rock Mech. Min. Sci.* **2019**, *122*, 104059. [CrossRef]
60. Mehrmashhadi, J.; Chen, Z.; Zhao, J.; Bobaru, F. A stochastically homogenized peridynamic model for intraply fracture in fiber reinforced composites. *Compos. Sci. Technol.* **2019**, *182*, 107770. [CrossRef]
61. Colpo, A.B. Application of the Discrete Element Method in the Simulation of the Damage Process in Materials. Ph.D. Thesis, Federal University of Pampa, Alegrete, Brazil, 2016.

62. Carpinteri, A. *Mechanical Damage and Crack Growth in Concrete: Plastic Collapse to Brittle Fracture*; Springer: Dordrecht, The Netherlands, 1986. [CrossRef]
63. Carpinteri, A.; Marenga, C.; Savadori, A. Ductile-brittle transition by varying structural size. *Eng. Fract. Mech.* **1985**, *21*, 263–271. [CrossRef]
64. Carpinteri, A. Cusp catastrophe interpretation of fracture instability. *J. Mech. Phys. Solids* **1989**, *37*, 567–582. [CrossRef]
65. Carpinteri, A.; Colombo, G. Numerical analysis of catastrophic softening behaviour (snap-back instability). *Comput. Struct.* **1989**, *31*, 607–636. [CrossRef]
66. Birck, G.; Rinaldi, A.; Iturrioz, I. The fracture process in quasi-brittle materials simulated using a lattice dynamical model. *Fatigue Fract. Eng. Mater. Struct.* **2019**, *42*, 2709–2724. [CrossRef]
67. Kosteski, L.E.; Iturrioz, I.; Lacidogna, G.; Carpinteri, A. Size effect in heterogeneous materials analyzed through a lattice discrete element method approach. *Eng. Frac. Mech.* **2020**, *232*, 107041. [CrossRef]
68. Grosse, C.U.; Ohtsu, M. *Acoustic Emission Testing*; Springer: Berlin/Heidelberg, Germany, 2008.
69. Ohtsu, M. The history and development of acoustic emission in concrete engineering. *Mag. Concr. Res.* **1996**, *48*, 321–330. [CrossRef]
70. De Sutter, S.; Verbruggen, S.; Tysmans, T.; Aggelis, D.G. Fracture monitoring of lightweight composite-concrete beams. *Compos. Struct.* **2017**, *167*, 11–19. [CrossRef]
71. Barile, C.; Casavola, C.; Pappalettera, G.; Vimalathithan, P.K. Acousto-ultrasonic evaluation of interlaminar strength on CFRP laminates. *Compos. Struct.* **2019**, *208*, 796–805. [CrossRef]
72. Colpo, A.B.; Kosteski, L.E.; Iturrioz, I. The size effect in quasi-brittle materials: Experimental and numerical analysis. *Int. J. Damage Mech.* **2017**, *26*, 395–416. [CrossRef]
73. Kosteski, L.E.; Iturrioz, I.; Friedrich, L.F.; Lacidogna, G. A study by the lattice discrete element method for exploring the fractal nature of scale effects. *Sci. Rep.* **2022**, *12*, 16744. [CrossRef]
74. Kosteski, L.E.; Friedrich, L.F.; Costa, M.M.; Bremm, C.; Iturrioz, I.; Xu, J.; Lacidogna, G. Fractal scale effect in quasi-brittle materials using a version of the discrete element method. *Fractal Fract.* **2024**, *8*, 678. [CrossRef]
75. Zohuri, B. Principles of the Dimensional Analysis. In *Dimensional Analysis Beyond the Pi Theorem*; Springer: Cham, Switzerland, 2017. [CrossRef]
76. Barenblatt, G.I. *Scaling*; Cambridge University Press: Cambridge, UK, 2003. [CrossRef]
77. Buckingham, E. On physically similar systems: Illustrations of the use of dimensional equations. *Phys. Rev.* **1914**, *4*, 345–376. [CrossRef]
78. Zhu, X.; Joyce, J.A. Review of fracture toughness (G, K, J, CTOD, CTOA) testing and standardization. *Eng. Frac. Mech.* **2012**, *85*, 1–46. [CrossRef]

Disclaimer/Publisher's Note: The statements, opinions and data contained in all publications are solely those of the individual author(s) and contributor(s) and not of MDPI and/or the editor(s). MDPI and/or the editor(s) disclaim responsibility for any injury to people or property resulting from any ideas, methods, instructions or products referred to in the content.